# Growth-induced self-organization in bacterial colonies

You, Z.

# Chapter 3

# Geometry and mechanics of freely expanding colonies

The ability of forming biofilms is a robust and widely observed property across different bacterial species [50]. Despite the extraordinary diversity within prokaryotic microorganisms, nearly all bacteria, either as single species or in a community, possess the necessary biomolecular "toolkit" to colonize a range of natural or synthetic surfaces through autonomous production of extracellular matrix (ECM) [47]. Starting from a single bacterium, the colony gradually colonize the surroundings through a series of well-regulated protocols. The first step is to extend its territory with a monolayer expansion. With a solid ground, it invades the third dimension by squeezing cells out of the monolayer, and subsequently forms a multilayered structure and then a mature biofilm [43–47]. In all these processes, mechanical forces play a very important role.

In this chapter, we will explore the spatial organization and mechanical properties in a freely expanding monolayer–the "childhood" of a biofilm. Using molecular dynamics simulations and continuous modeling, we demonstrate that the dynamics of the freely expanding monolayer is dominated by the competing effects of cell slenderness and cell growth. On the one hand, passive steric repulsion between the rod-shaped cells tends to align the cell axes, and promotes local nematic order. On the other hand, cell elongation along the axis generates an extensile active stress in the colony, which can bend the director and create a distortion. The competition between the passive and growth-induced active forces results in a complex internal dynamics as well as the emergence of coherent structures (Figs. 3.1a–d) reminiscent of those observed in active liquid crystals [29, 88–91]. Especially, the expanding colony self-organizes into a "mosaic" of nematic microdomains, whose sizes are exponentially distributed, with a characteristic length scale proportional to the square root of the ratio between the system orientational stiffness and the magnitude of the extensile active

stress. Both active and passive forces scale linearly with the cell density. Therefore, despite the colony being denser in the center than at the periphery, such an inherent length scale remains uniform throughout the system. Finally, to assess the significance of our theoretical model, we compare our predictions with experiments on freely growing *E. coli* microcolonies (Fig. 3.1). Whereas the statistics of our experiments are not sufficient to make conclusive statements, we do not find obvious discrepancies with our theoretical model. In contrast, the agreement between theory and experiments justifies some degree of optimism and creates promising ground for future experimental research.

## 3.1 Stochastic geometry

We use the hard-rod model introduced in section 2.1 to simulate the freely expanding monolayer. We assume the colony to be perfectly quasi-two-dimensional, i.e. cells only move in the $xy$-plane, and the force components in the third dimension have no effects on the in-plane dynamics. To do so, we manually set $z_i = d_0/2$ and $q_{iz} = 0$ for all cells and at all times. Equations 2.1 and 2.2 have been numerically integrated using the following set of parameter values: $d_0 = 1\,\mu$m, $Y_c = 4$ MPa, and $\zeta = 200$ Pa h [62]. The division length $l_d$ varies from $2\,\mu$m to $5\,\mu$m, and the growth rate varies from $1\,\mu$m/h to $10\,\mu$m/h. The integration is performed with a time step $\Delta t = 0.5 \times 10^{-6}$ h. Each simulation starts with one randomly oriented cell and stops when the total length of the cells in the colony, i.e., $\mathcal{L} = \sum_i^N (l_i + d_0)$, reaches the value $37500\,d_0$, such that colonies with different $l_d$ values have approximately the same colony area at the end of the simulation. We can rescale the length by the cell diameter $d_0$ and the time by $\zeta/Y_c$. In these units, our hard-rod model has only two free parameters: $l_d/d_0$, which represents the cell slenderness or aspect ratio, and the rescaled growth rate $g\zeta/(Y_c d_0)$. In the remainder of this chapter, all results are presented in terms of dimensionless quantities, unless otherwise specified.

Figure 3.1 shows the typical configurations observed at the early stages of colonization both *in vitro* and *in silico*. Along the colony boundary, cells are predominantly tangentially aligned, as a consequence of torque balance. As the forces experienced by the peripheral cells are radial, these cells must orient either tangentially or normally with respect to the boundary in order for the torque acting on them to vanish. Normal alignment

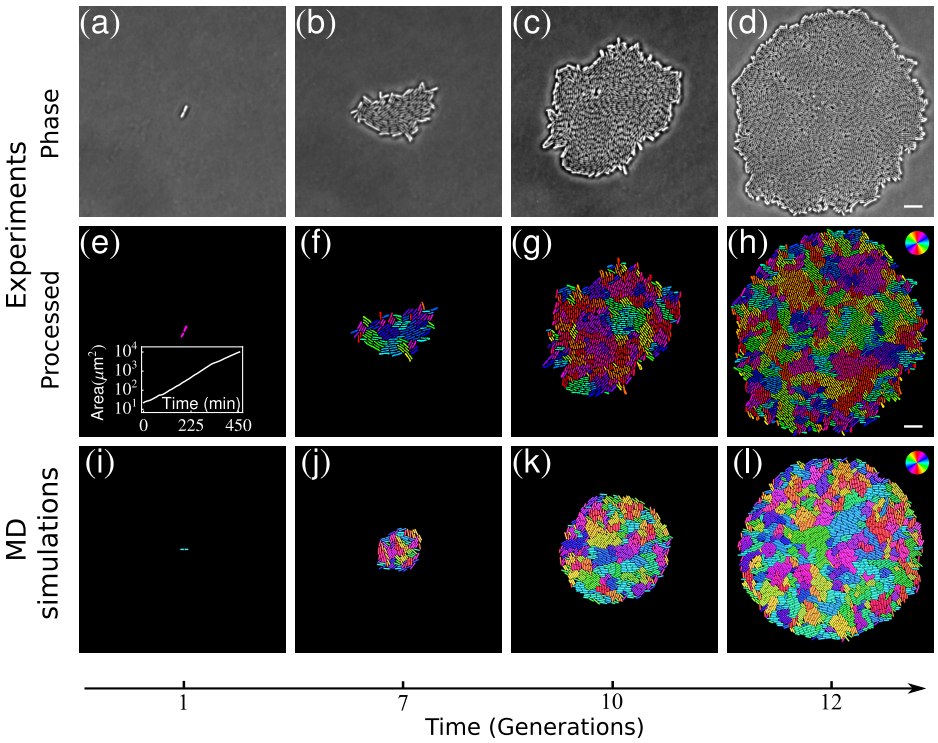


**Figure 3.1. Growth of a bacterial colony.** (a)–(d) Phase-contrast micrographs at different time points capture the growth of a single cell of nonmotile strain of *Escherichia coli* (strain NCM 3722 delta-motA) to a two-dimensional colony under free boundary conditions. The scale bar corresponds to 10 $\mu$m. The cell doubling time was $43.5 \pm 2.2$ minutes. After 12 generations (d), the colony was observed to escape into the third dimension and form a second bacterial layer. (e)–(h) Image analyzed snapshots of (a)–(d), capturing the emergence of local orientational order within the growing bacterial colony, represented by differently colored microdomains. Cells are color-coded by the orientation of the domains they belong to, as described in the color wheel in panel (h). The inset in panel (e) plots the area of the growing bacterial colony over time, showing the exponential growth of cells in the colony. (i)–(l) The corresponding time points during the growth of the bacterial colony obtained using molecular dynamics simulations. Cells are color-coded with the same method as in panels (e)–(h). By varying the aspect ratio of the cells (length/width) between 1.5 and 4, different physiological states were simulated.

is, however, unstable; therefore, most of the peripheral cells are oriented tangentially. This tangential alignment has also been observed in several other studies [63, 65]. In bulk of the colony, the emergence of local nematic order is conspicuous throughout the system; however, this does not propagate across the colony but remains confined to a set of microscopic domains. These nematic domains, or "patches," are separated from each other by fracture lines reminiscent of grain boundaries in crystals [92, 93]. We can then use these domains to characterize the geometrical properties of a growing bacterial colony and, hopefully can also infer the mechanical properties of such systems.

At first glance, these nematic domains show very complicated spatial-temporal dynamics. As the colony evolves, the domains grow, merge, buckle, and break apart, in a complex sequence of morphological and topological transformations. These phenomena suggest a chaotic nature of the freely expanding monolayer. Despite the complex dynamics, these domains exhibit very robust statistical properties. Figure 3.2 shows three examples of proliferating colonies of cells, each with different $l_d$ values and, hence, different cell aspect ratios. The typical domain area, as we can see, increases with the cell aspect ratio. Although the microdomains possess local orientational order, no preferential orientation was observed at the scale of the colony, suggesting that the colony itself is globally isotropic. The absence of the global orientational order can be ascribed to the inherent instability of the domains, which continuously deform and fracture under the effect of growth-induced stress. The typical domain area then represents not only the coherent length scale of orientational order but also the length scale at which the internal stresses compromise.

To quantify the emergent geometry of microdomains in a colony, we apply a customized domain segmentation algorithm. Two cells are considered to belong in the same domain if they are in contact, and their relative orientation differed by less than 3%. Although decomposition of a colony depends on the chosen threshold, the overall nature of the geometry and the emergent trends identified through different quantifiable parameters are generally robust and independent of the chosen threshold. By using this algorithm, we can then identify domains; measure their positions, orientations, areas *et al.*; and get statistics of these quantities.

A central quantity to characterize the geometry of a colony is the probability density of the area of these microdomains, $P(A)$. This is shown in Fig. 3.3a for colonies with different $l_d$ values. The frequency of

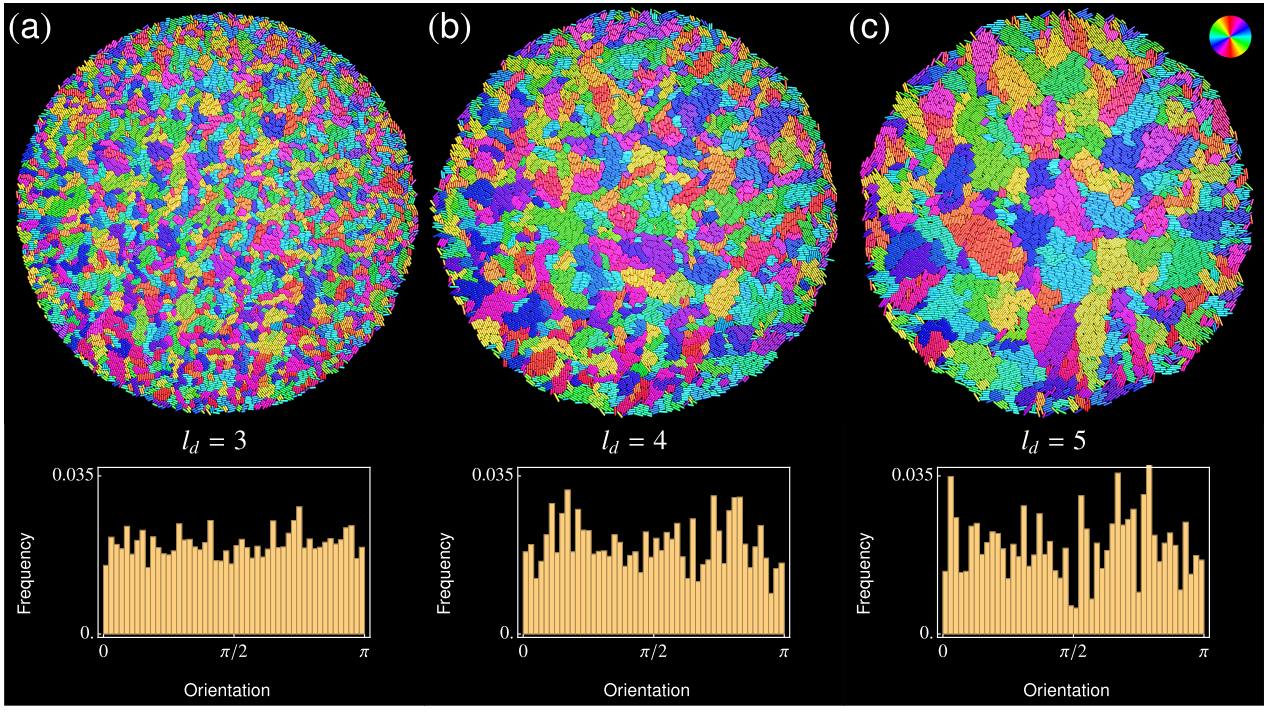


**Figure 3.2. Emergence of nematic domains in proliferating bacterial colonies.** (a)–(c) Examples of nematic microdomains in simulated bacterial colonies for various division lengths ($l_d$ = 3, 4, 5, in units of the cell diameter $d_0$). Cells are colored with the same method as in Fig. 3.1. Upon increasing the division length, the typical area of the domains increases progressively. Inside a domain, the cells are highly aligned, while there is no preferential orientation at the scale of the entire colony, as confirmed by the probability distribution of cell orientations (corresponding panels in the lower row).

domains with area $A$ decreases with $A$ and, for sufficiently large $A$ values, $P(A)$ approaches the exponential distribution:

$$P(A) \sim \exp\left(-\frac{A}{A^*}\right) , \tag{3.1}$$

where $A^*$ is a characteristic area scale proportional to the average domain area. For small $A$ values, the distribution slightly deviates from the exponential form. This range corresponds to the boundary of the colony where, because of the sudden drop in packing fraction, domains are very small or consist of single cells. Although small domains seem to be outnumbered large domains in the exponential region, they actually occupy relatively small area in the whole colony, as can be obviously seen in Fig. 3.2. This is because a large domain typically is as large as tens or even hundreds of small domains altogether. For this reason, it's fair to say that the domain size is exponentially distributed in a growing colony.

We will now quantify the spatial dependence of the domains. First of all, we notice that a sufficiently large colony has a rotational symmetry about the colony center. This rotational symmetry is commonly shared by all geometrical and mechanical quantities, which then depend exclusively on $r$, the distance from the colony center. We calculate the average domain area restricted to an annular strip, of width $5d_0$, and located at distance $r$ from the center of the colony, i.e., $\langle A \rangle_r$ (Fig. 3.3b). The local domain area is uniform in the bulk of the colony, for a given cell aspect ratio, before dropping to zero at the boundary, where the colony is more disordered. In turn, the average domain area in the bulk $\langle A \rangle$ is strongly affected by the division length $l_d$. This is visibly conspicuous in Fig. 3.2. Increasing $l_d$ makes the cells, on average, more slender, resulting in larger and more stable domains, as revealed by the plot in Fig. 3.3c. More interestingly, increasing the growth rate $g$ has the opposite effect and causes a drop in the domain area (Fig. 3.3d). All data in Fig. 3.3, as well as those in Figs. 3.4, 3.5, 3.6, and 3.7 are obtained by averaging over 480 runs. All simulation results in this chapter are obtained by analyzing the configurations of the colonies at which the simulations stop, unless otherwise specified. The error bars show the standard deviations of the 480 samples with respect to the mean values.

The results reported in this section quantitatively demonstrate that the spatial organization of the microdomains in expanding bacterial colonies is regulated by the competing effects of the cell aspect ratio and the growth rate. These effects can ultimately be ascribed to the mechanical proper-

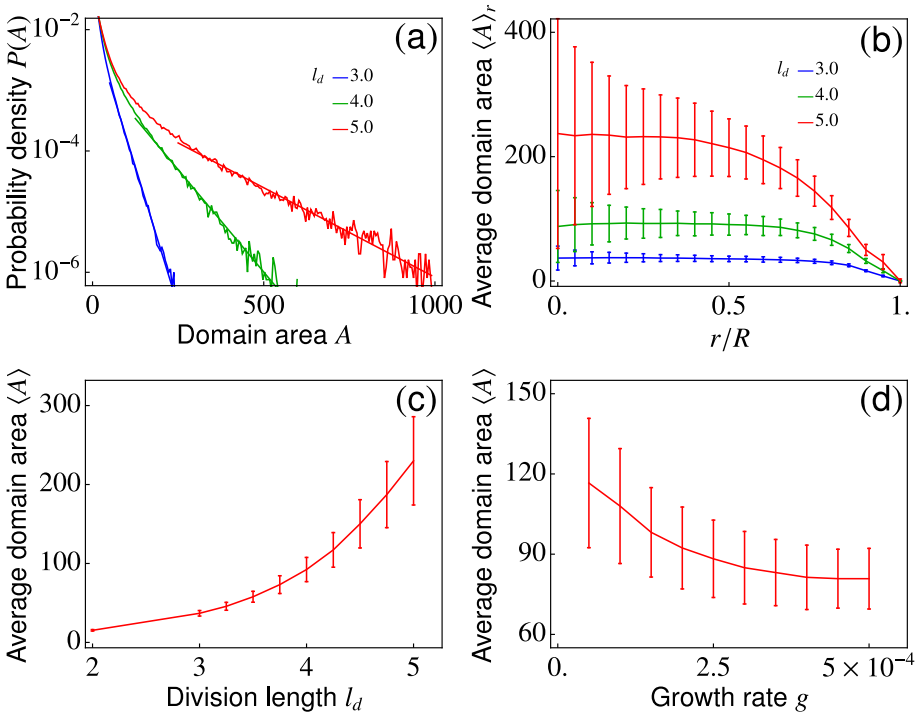


**Figure 3.3. Geometry of nematic microdomains in bacterial colonies.** (a) Probability distributions of domain area, $P(A)$, for various division length $l_d$. The domain area follows the exponential distribution $P(A) \sim \exp(-A/A^*)$, with $A^* = 54.3$, 148.2, and 338.8, respectively, which increases with the division length $l_d$. (b) The average domain area at a distance $r$ from the center of the colony, showing that the area of the domains is found to be constant in the bulk of the colony and drops to zero at the boundary. (c,d) The bulk domain area $\langle A \rangle$ (c) increases with the division length $l_d$ and (d) decreases with the growth rate $g$. Here, $\langle A \rangle$ is calculated by averaging the areas of all domains within the range $0 \leq r \leq R/2$, with $R$ the colony radius. All results shown in panels (a)–(c) correspond to a fixed growth rate of $g = 0.0002$ (or $4\mu$m/h in physical units), while panel (d) represents simulation results with a fixed division length $l_d = 4$.

ties of the system, as we explain in the next section. We stress here that our approach does not aim to faithfully reproduce all the experimental details but rather to provide a conceptual key for understanding certain geometrical and mechanical properties, with the help of a minimal model comprising a single fitting parameter: i.e., the timescale $\tau = \zeta/Y$. Other properties, such as the roughness of the colony edge and smoother variation in the orientation of neighboring domains, are not well captured by our simple model and would require a more sophisticated construction, accounting for the adhesive interaction between neighboring cells, the flexibility of the cell membrane, and more specific cell-substrate interactions [65]. Unfortunately, this would imply a cost in terms of free parameters and reduced simplicity in the interpretation of the numerical results.

## 3.2 Mechanics

The domain geometry in a proliferating bacterial colony is determined by the interplay between two competing forces: steric repulsion between neighboring cells and the extensile stresses due to cell growth. While cell-cell steric repulsion favors alignment, the emergent extensile stresses due to the growth within a restricted environment (i.e., the space delimited by the neighboring domains) tend to deform and eventually fracture a domain. Both of these effects are due to contact forces and are, therefore, enhanced by the local packing fraction $\phi$.

To clarify this concept, we measure the local packing fraction $\phi(r,t) = \sum_i a_i(t)/\mathcal{A}_r$, where $a_i(t)$ is the area of the $i$th cell, located at time $t$ inside a thin annulus of radius $r$, width $5d_0$, and area $\mathcal{A}_r$, centered at the colony center. As mentioned before, the colony has a radial symmetry; hence, the local packing fraction depends exclusively on the distance $r$ from the center. Figure 3.4a shows that at any given time, the packing fraction decreases monotonically with $r$. As bacteria duplicate and progressively colonize the surrounding space, the local packing fraction increases with time throughout the system while maintaining a characteristic spatial profile that smoothly interpolates between a time-dependent maximum $\phi(0,t) = \phi_{\max}(t)$, at the center of the colony, and a time-independent minimum, $\phi(R,t) = \phi_c$, at the edge ($R$ being the colony radius). The quantity $\phi_c \approx 1$ is the critical packing fraction at which the cells first start to compress each other. In close proximity of the edge of the colony, $\phi < \phi_c$, and the contact forces tend to reorient the cells with-

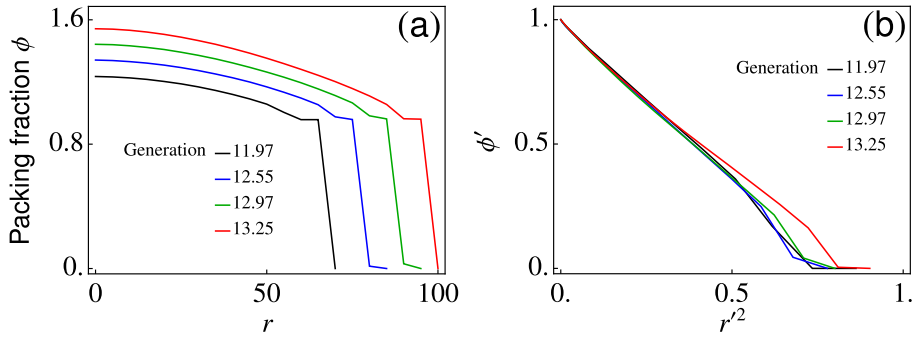


**Figure 3.4.** (a) Spatial dependence of the packing fraction for different ages of colonies. (b) The rescaled packing fraction $\phi' = [\phi(r) - \phi(R)]/[\phi(0) - \phi(R)]$ versus $r'^2 = (r/R)^2$. All the curves collapse on the same line as demanded by Eq. 3.2. The growth rate and the division length are fixed, i.e., $g = 0.0002$ and $l_d = 4$. The packing fraction $\phi$ is averaged over a thin annulus of radius $r$ and width $5d_0$, centered at the colony center. In all results presented, the length is expressed in units of the cell width, $d_0$, and time in units of the timescale $\zeta/Y_c$ defined in Eqs. 2.2.

out compressing them, leading to an abrupt drop in the packing fraction. Upon rescaling the packing fraction by $\phi(0) - \phi(R)$ and the distance $r$ by the colony radius $R$, the spatial dependence of the pacing fraction can be described, at any time, by a simple quadratic law:

$$\frac{\phi(r) - \phi(R)}{\phi(0) - \phi(R)} = 1 - \left(\frac{r}{R}\right)^2 , \tag{3.2}$$

as illustrated in Fig. 3.4b. As we analytically prove in section 3.3, such a density profile originates from the balance between growth-induced pressure and drag from the substrate.

The tendency of the cells to align with each other is driven by the local steric interactions and can be conceptualized in the framework of Frank elasticity [77], starting from the free-energy density:

$$f_F = \frac{1}{2} k_F |\nabla \boldsymbol{n}|^2 . \tag{3.3}$$

Here, $k_F$ is an orientational stiffness penalizing, in equal amounts, splay and bending deformations, and $\boldsymbol{n}$ is the local nematic director corresponding to the average orientation of the bacteria in a local region. Any departure from the uniformly aligned configuration causes restoring forces

proportional to the field $\boldsymbol{h} = -\delta/\delta\boldsymbol{n} \int \mathrm{d}A\, f_F = k_F \nabla^2 \boldsymbol{n}$ [77]. As a consequence of growth, each cell further acts as an extensile force dipole that pushes away its neighbors along the $\pm\boldsymbol{n}$ direction. This collectively gives rise to an internal stress of the form

$$\boldsymbol{\sigma} = -p\boldsymbol{I} + \alpha \left( \boldsymbol{nn} - \frac{1}{2}\boldsymbol{I} \right) , \tag{3.4}$$

where $p$ is the pressure, $\boldsymbol{I}$ the identity matrix, and $\alpha$ the deviatoric active stress [94, 39]. In the most general case, the three quantities $k_F$, $p$, and $\alpha$, appearing in Eqs. 3.3 and 3.4, are functions of the local packing fraction and the nematic order parameter, in addition to the cell aspect ratio and the growth rate.

Equations 3.3 and 3.4 identify a fundamental length scale $\ell_\mathrm{a} = \sqrt{k_F/|\alpha|}$, proportional to the distance at which the passive restoring forces arising in the system, in response to a local distortion, balance the active forces that cause the nematic director to rotate [29]. This length scale plays a pivotal role in the mechanics of active nematic liquid crystals [95–98, 78] and, as we clarify later, determines their collective behavior and mechanical properties. In the following, we demonstrate that, in a growing colony of nonmotile cells, the inherent length scale $\ell_\mathrm{a}$ determines the geometrical properties of the microdomains in such a way that $\langle A \rangle \sim \ell_\mathrm{a}^2$. For this purpose, we measure the orientational stiffness $k_F$ and the stresses $\boldsymbol{\sigma}$ exerted inside the colony. The stress experienced by the $i$th cell, $\boldsymbol{\sigma}_i$, can be calculated from the virial expansion [38]:

$$\boldsymbol{\sigma}_i = \frac{1}{a_i'} \sum_j \boldsymbol{r}_{ij}\, \boldsymbol{F}_{ij} , \tag{3.5}$$

where $a_i' = a_i/\phi$ is the effective area occupied by the $i$th cell. We express the tensor in the basis of the nematic director and its normal $\boldsymbol{n}^\perp = (-n_y, n_x)$, namely,

$$\boldsymbol{\sigma} = \sigma_\parallel \boldsymbol{nn} + \sigma_\perp \boldsymbol{n}^\perp \boldsymbol{n}^\perp + \tau(\boldsymbol{nn}^\perp + \boldsymbol{n}^\perp \boldsymbol{n}) . \tag{3.6}$$

Figure 3.5a shows a plot of the various components of the stress tensor versus the packing fraction, given by Eq. 3.5. As expected, the normal stresses $\sigma_\parallel$ and $\sigma_\perp$ increase with the packing fraction and, at any finite packing fraction, are such that $|\sigma_\parallel| > |\sigma_\perp|$, as a consequence of the anisotropic cell growth. The shear stress $\tau$, on the other hand, is always negligible because of the absence of lateral friction between the cells.

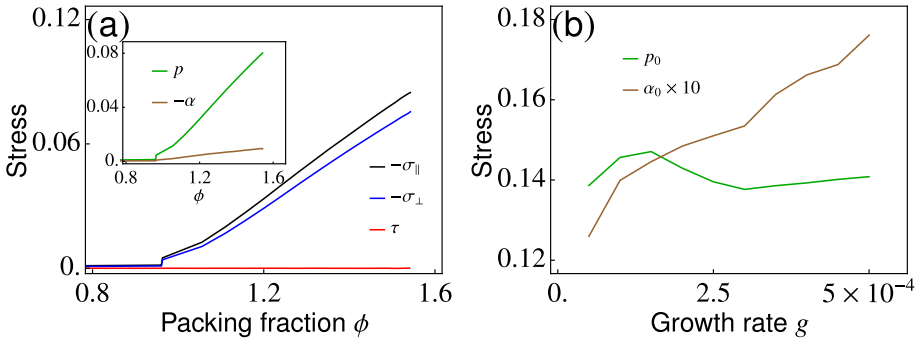


**Figure 3.5.** (a) Different components of the internal stress $\boldsymbol{\sigma}$ as functions of packing fraction $\phi$. The normal stress parallel to the director $\boldsymbol{n}$, $|\sigma_\parallel|$, is larger than that perpendicular to it, i.e., $|\sigma_\perp|$. Both $|\sigma_\parallel|$ and $|\sigma_\perp|$ are piecewise linear functions of $\phi$, while the shear component $\tau$ vanishes. The normal components of stress can be rearranged into a hydrostatic pressure $p$ and an extensile active stress $\alpha$, and both increase linearly with the packing fraction (inset). The simulation parameters are the same as those in Fig. 3.4. Again, $\boldsymbol{\sigma}$ is averaged over a thin annulus of radius $r$ and width $5d_0$, centered at the colony center. (b) The pressure is independent of growth rate $g$, while the active stress increases with $g$. Here, $l_d = 4$ is fixed.

Note that both $\sigma_\parallel$ and $\sigma_\perp$ are negative because of the extensile nature of the growth-induced forces. The dependence of the normal stresses on the packing fraction is piecewise linear: For $\phi < \phi_c$, the contact forces can be relieved by rotations and repositioning of the cells, and $\sigma_\parallel \approx \sigma_\perp \approx 0$; however, for $\phi > \phi_c$, the cells in the bulk are tightly packed, and internal stresses build up as the packing fraction increases. Setting $\tau = 0$ in Eq. 5.28 and taking $\boldsymbol{n}^\perp\boldsymbol{n}^\perp = \boldsymbol{I} - \boldsymbol{nn}$, one can rearrange the stress tensor in the form

$$\boldsymbol{\sigma} = -\frac{|\sigma_\parallel + \sigma_\perp|}{2}\,\boldsymbol{I} + (\sigma_\parallel - \sigma_\perp)\left(\boldsymbol{nn} - \frac{1}{2}\,\boldsymbol{I}\right) . \tag{3.7}$$

Comparing this with Eq. 3.4 straightforwardly yields $p = (|\sigma_\parallel + \sigma_\perp|)/2$ and $\alpha = \sigma_\parallel - \sigma_\perp$. Together with the numerical results summarized in Figs. 3.5a–b, this implies

$$p = p_0(\phi - \phi_c) , \qquad \alpha = -\alpha_0|\phi - \phi_c| , \tag{3.8}$$

as long as $\phi > \phi_c$. Not unexpectedly, the longitudinal growth of the cells gives rise to an extensile (i.e., $\alpha < 0$) active stress that decreases monotonically with the distance from the center of the colony. The prefactors

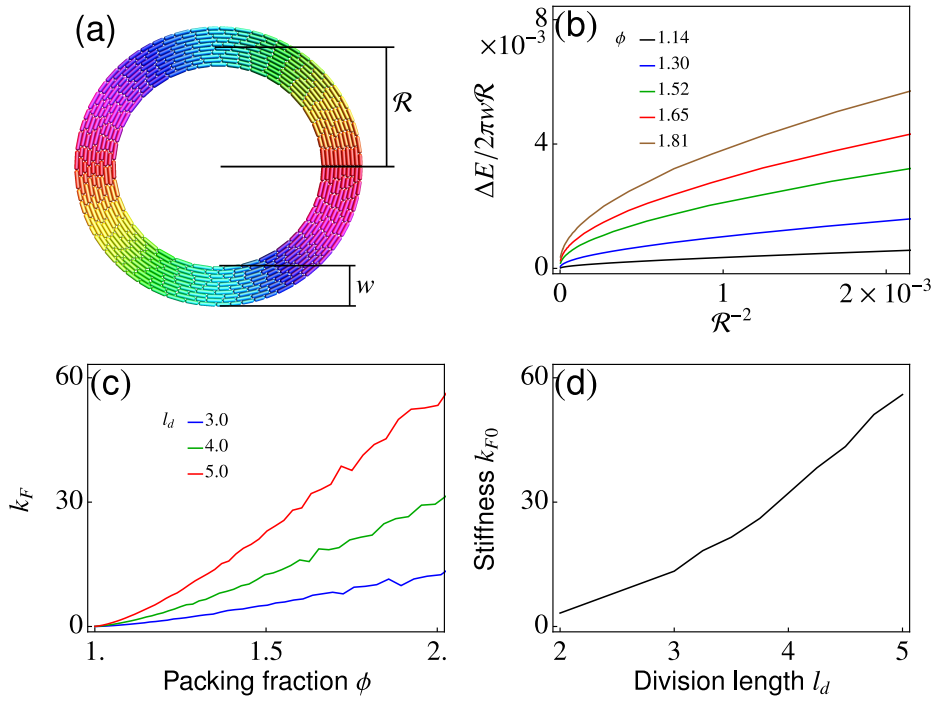


**Figure 3.6.** (a) The ring-shaped colony we used to measure the bending stiffness $k_F$. It has a radius $\mathcal{R}$ and a width $w$. Cells are colored by their orientations according to the color wheel in Fig. 3.1. (b) Difference of energy density (energy per unit area) between the straight channel and a ring-shaped channel of radius $\mathcal{R}$, as a function of $\mathcal{R}^{-2}$. (c) The orientational stiffness $k_F$ increases linearly with the packing fraction at fixed $l_d$. (d) The prefactor of the linear fit, $k_{F0}$, increases with the division length $l_d$.

$p_0$ and $\alpha_0$ are plotted in Fig. 3.5b as a function of the growth rate $g$. The active stress $\alpha_0$ increases monotonically with $g$, while $p_0$ is essentially independent.

In order to estimate the orientational stiffness $k_F$, we manually arrange our *in silico* bacterial colony inside an annular channel of width $w = 10d_0$ and radius $\mathcal{R}$ (Fig. 3.6a, $w \ll \mathcal{R}$), as well as in a straight one of the same width and lengthed $2\pi\mathcal{R}$. In both configurations, the energy associated with the Hertzian contacts can be measured as: $E = (2/5)\, Y_c d_0^{1/2} \sum_{\langle ij \rangle} h_{ij}^{5/2}$, where the summation runs over all the pairs of cells in contact with each other. By comparing how the energy den-

sity changes with the curvature of the channel, we can infer the orientational stiffness. Figure 3.6b shows a plot of the difference $\Delta E = E(\phi, \mathcal{R}) - E(\phi, \infty)$ between the energy of a bent channel with radius $\mathcal{R}$ and a straight channel (both have a length $2\pi\mathcal{R}$), normalized by the area $2\pi w\mathcal{R}$ of the channel, as a function of the squared curvature $\kappa^2 = 1/\mathcal{R}^2$. From Eq. 3.3, it follows that $k_F = \partial_{\kappa^2}\Delta E/(2\pi w\mathcal{R})|_{\kappa=0}$. As shown in Fig. 3.6c, at fixed division length, the orientational stiffness $k_F$ increases linearly with the packing fraction, i.e., $k_F = k_{F0}(\phi - \phi_c)$. Furthermore, increasing the slenderness of the cells makes the colony orientationally stiffer (Fig. 3.6d).

Combining the measurements of the extensile active stress and the orientational stiffness, we are finally able to formulate a scaling law for

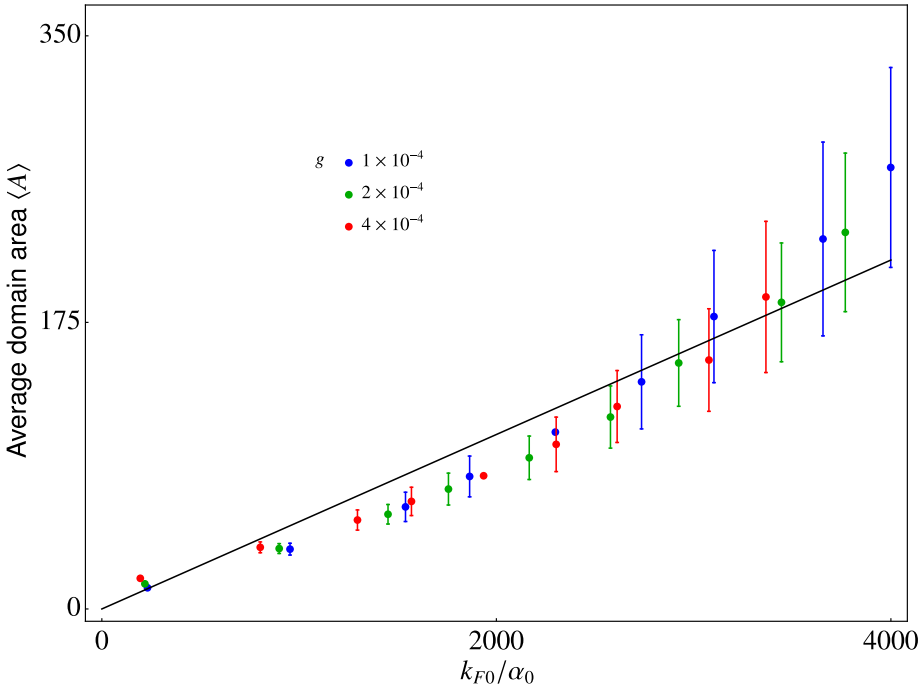


**Figure 3.7.** The average domain area $\langle A \rangle$ is approximately proportional to $k_{F0}/\alpha_0$, for various combinations of growth rate and division length. We choose three growth rates (identified by colors), and for each growth rate, we gradually increase the division length from $l_d = 2$ to $l_d = 5$, corresponding to different data points with the same color.

the area of the nematic microdomains comprising our simulated bacterial colonies. Namely,

$$\langle A \rangle \sim \frac{k_F}{|\alpha|} \,, \tag{3.9}$$

in agreement with our numerical data (Fig. 3.7). In summary, bacterial colonies freely growing on a two-dimensional frictional substrate spontaneously organize into a "mosaic" of microdomains consisting of highly aligned cells. The domains are randomly oriented so that the colony is globally isotropic and circularly symmetric at the global scale, while their areas are exponentially distributed, as indicated in Eq. 3.1. Such a distribution results from the competition between passive steric forces, which favor local alignment, and the extensile active forces originating from the cell growth. These forces balance at the length $\ell_{\mathrm{a}} = \sqrt{k_F/|\alpha|}$, resulting in a characteristic domain area that scales as $\ell_{\mathrm{a}}^2$. Remarkably, both the orientational stiffness $k_F$ and the extensile active stress $\alpha$ scale linearly with the packing fraction $\phi$. Consequently, $k_F/\alpha = k_{F0}/\alpha_0$, so the average domain area is uniform throughout the colony (Fig. 3.3b). Such a cancellation of the dependence is intriguing: It is presumably specific to the type of interactions chosen here, which we do not expect to hold in general. Including the bending elasticity of the cells could, for instance, change the packing fraction dependence of $k_F$ and $\alpha$, resulting in a space-dependent active length scale. Yet, the mechanism described here and summarized by Eq. 3.9 is general and does not depend on the details of the model.

## 3.3 Continuum theory

In this section, we demonstrate that much of the behavior previously described can be quantitatively captured in the realm of continuum mechanics by means of a suitable extension to the hydrodynamic equations of active nematic liquid crystals. Here, we introduce a comprehensive hydrodynamic framework, incorporating the density effects described in the previous section as well as the deviatoric active stresses in the colonization dynamics.

An expanding bacterial colony can be described in terms of the material fields $\rho$, $\boldsymbol{v}$, and $\boldsymbol{Q}$, representing, respectively, the cell density, velocity, and the nematic order. The dynamics of these fields is then governed by

the following hydrodynamic equations:

$$\frac{D\rho}{Dt} = k_g\rho + \mathcal{D}\nabla^2\rho \,, \tag{3.10a}$$

$$\frac{D(\rho\boldsymbol{v})}{Dt} = \nabla\cdot\boldsymbol{\sigma} - \xi\rho\boldsymbol{v} \,, \tag{3.10b}$$

$$\frac{D\boldsymbol{Q}}{Dt} = \lambda S\boldsymbol{u} + \boldsymbol{Q}\cdot\boldsymbol{\omega} - \boldsymbol{\omega}\cdot\boldsymbol{Q} + \gamma^{-1}\boldsymbol{H} \,, \tag{3.10c}$$

modified from Eqs. 2.4, with an additional term $k_g\rho$ (in Eq. 3.10a) representing an exponential growth of the colony total mass at a rate $k_g$ (proportional to the length extension rate $g$ used in section 3.1). Further details of the continuum theory can be found in section 2.2. The internal stresses $\boldsymbol{\sigma}$ is similar to that of an active nematics:

$$\boldsymbol{\sigma} = -p\boldsymbol{I} + \alpha\boldsymbol{Q} - \lambda S\boldsymbol{H} + \boldsymbol{Q}\cdot\boldsymbol{H} - \boldsymbol{H}\cdot\boldsymbol{Q} \,, \tag{3.11}$$

where the second term represents the extensile active stress introduced by the cell growth. Now, consistent with the results of our hard-rod model presented in section 3.2, we encode a specific density dependence in the quantities $p$, $\alpha$, and $L_1 \sim k_F$. We introduce the packing fraction $\phi = \rho/\rho_c$, where $\rho_c$ is the density at which cells become closely packed and start to transmit stress. Based on these considerations, we set

$$p = p_0\,(\phi - 1) \,, \quad \alpha = -\alpha_0\,(\phi - 1) \,, \quad L_1 = k_{F0}\,(\phi - 1) \,,$$

where $p_0$, $\alpha_0$, and $k_{F0}$ are positive constants. Furthermore, we take $\alpha_0 \sim k_g$ and keep $p_0$ independent of $k_g$, based on the results summarized in Fig. 3.5b. In our system of growing cells, orientational order is driven uniquely by the steric repulsion, and the system transitions to a nematic phase for large enough densities. We set $A_2 = A_0(\rho^* - \rho)/2$ and $A_4 = A_0\rho$, so the system has an equilibrium order parameter $S = \sqrt{1 - \rho^*/\rho}$, with a critical density $\rho^*$; hence, the colony is disordered for densities $\rho < \rho^*$, and it is nematic for $\rho > \rho^*$. In the following, we assume $\rho_c > \rho^*$ to reflect the earlier observation that, at very low density (i.e., at the boundary of the colony), the contact forces tend to reorient cells rather than compress them.

Equations 3.10 have been numerically solved using a finite difference approach on a $351 \times 351$ collocated grid. Figure 3.8 shows a typical configuration obtained for sufficiently large growth rates, in terms of the nematic

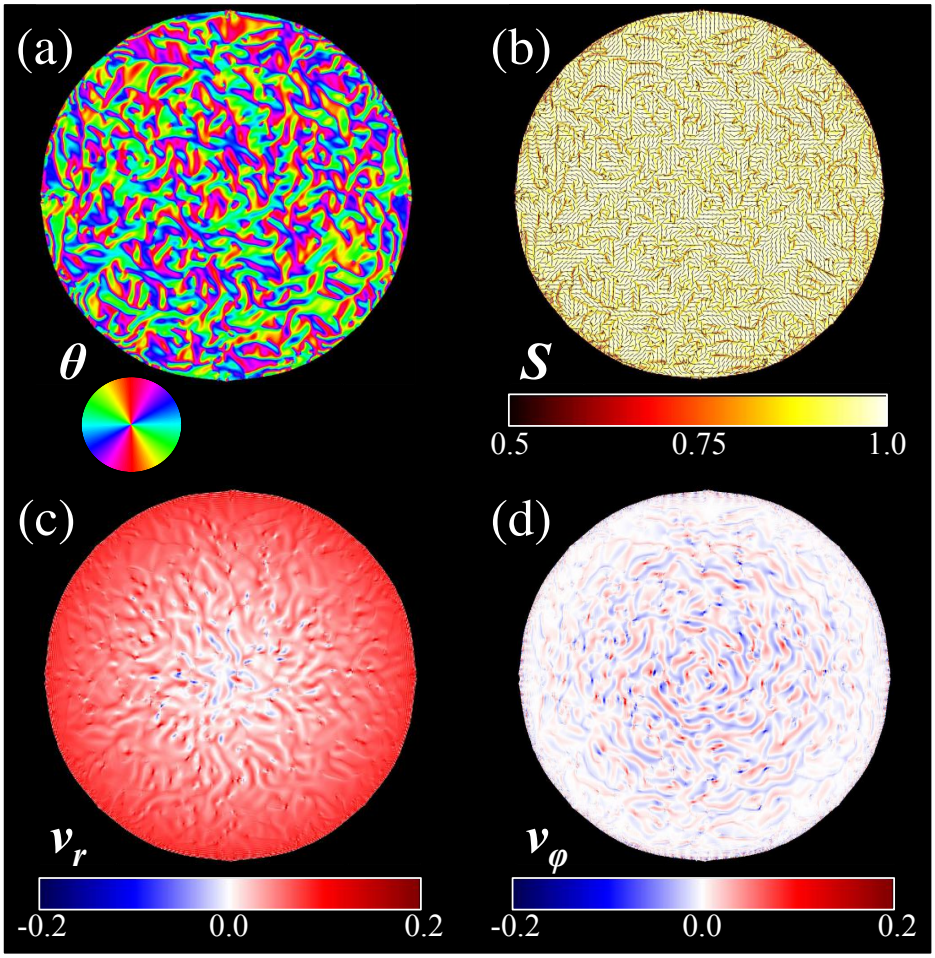


**Figure 3.8. Continuous Model.** (a) Snapshot of a typical configuration obtained from a numerical integration of Eqs. 3.10. Displayed here is the angle between the nematic director and the $x$ axis, colored using the same color scheme as in Fig. 3.1. (b) Director field (lines) superimposed on a color map of the nematic order parameter $S$. As for the hard-rod model, nematic order is approximatively uniform except at the boundary of the domains. (c) Radial and (d) tangent components of the velocity field, $v_r$ and $v_\varphi$. Along the radial direction, the flow is predominantly expansive because of the cell growth. On the other hand, there is no net circulation along the tangential direction.

director and order parameter (Fig. 3.8a and 3.8b) and velocity field (Fig. 3.8c and 3.8d). As for our hard-rod models, these consist of an ensemble of randomly oriented nematic domains, whose characteristic area remains uniform in the bulk of the colony. In order to make a quantitative comparison between our discrete and continuous models, we reconstruct the geometrical properties of the microdomains based on the following criterion. Given the orientation $\theta = \arctan(Q_{xy}/Q_{xx})/2$ of the nematic director, we define $\Theta$ as the coarse-grained $\theta$ field in which all values are sorted into bins; e.g., $2(n-1)\pi/m \leq \theta < 2n\pi/m \implies \Theta = (2n-1)\pi/m$ for $n = 1, 2, \ldots, m$ (with $n$ and $m$ both integers). This divides the colony into domains that can then be identified by labeling the connected components of the resulting two-dimensional matrix. We use a value of $m = 6$ here to reflect a typical $\theta$ change between two boundaries in the hard-rod model.

Figure 3.9 summarizes the results obtained from a numerical integration of Eqs. 3.10. As for the hard-rod model, the density decreases monotonically from the center of the colony, consistent with the quadratic law given by Eq. 3.2 (Fig. 3.9a). Here, we demonstrate that such a property originates from the interplay between growth-induced pressure and drag from the substrate. Under this hypothesis and assuming low Reynolds number, from Eq. 3.10b, one can approximate the momentum density in the Darcy-like form $\rho\boldsymbol{v} = -\mu\nabla\rho$, where $\mu = p_0/(\xi\rho_c)$ is a mobility coefficient. Using this relation in Eq. 3.10a yields the following moving boundary value problem for the colony density:

$$\partial_t\rho = \mu\nabla^2\rho + k_g\rho\ , \qquad |\boldsymbol{r}| < |\boldsymbol{R}|\ , \tag{3.12a}$$

$$\rho(\boldsymbol{R}, t) = \rho_c\ , \tag{3.12b}$$

$$\dot{\boldsymbol{R}} = -\mu\rho^{-1}\nabla\rho|_{\boldsymbol{r}=\boldsymbol{R}}\ , \tag{3.12c}$$

where we indicate with $\boldsymbol{R}$ the position of the boundary of the colony and with $\dot{\boldsymbol{R}} = \boldsymbol{v}(\boldsymbol{R})$ its velocity. Because of the circular symmetry of the colony at long times, $\boldsymbol{R} = R\hat{\boldsymbol{r}}$, and Eqs. 3.12 reduce to a Stefan problem with one spatial and one temporal variable [99]. At short times, density and pressure are still roughly uniform across the system, and growth results mainly in a radial expanding flow. Consistent with Eq. 3.10a, if $\rho(r,t) \approx$ const, then $\nabla\cdot\boldsymbol{v} = k_g$. Thus, assuming $v_\varphi = 0$, we get $v_r = k_g r/2$ and $R(t) = R(0)\exp(k_g t/2)$. The long time dynamics, on the other hand, is dominated by the internal diffusive currents. In this regime, $\rho(0,t) \gg \rho_c$

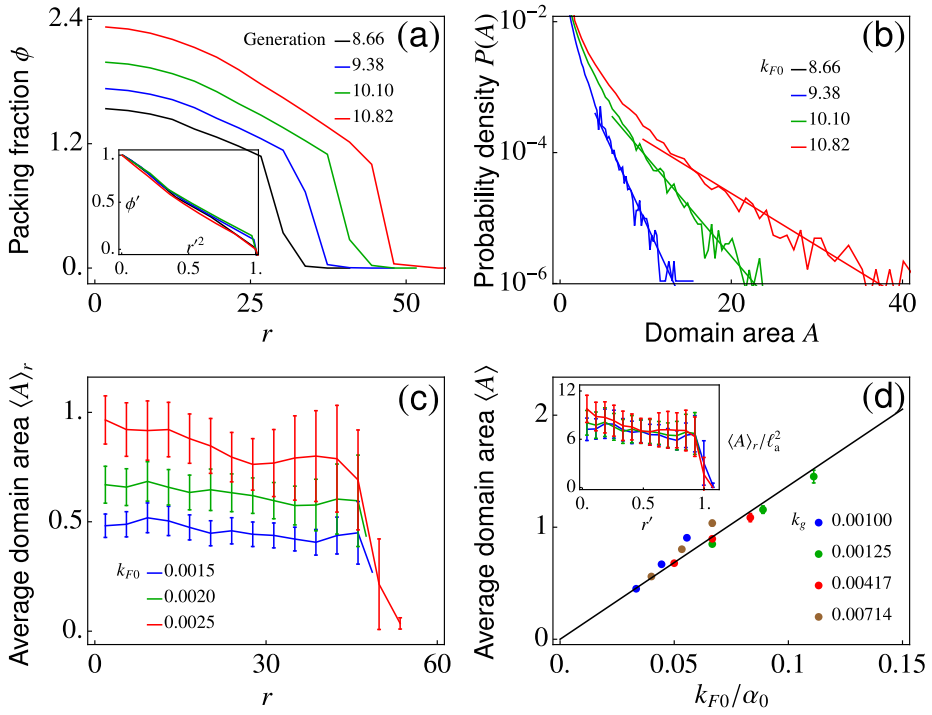


**Figure 3.9. Geometrical properties of continuous colonies.** (a) Spatial distribution of the packing fraction ($\phi = \rho/\rho_c$) for colonies of different ages, given by their generation. Similar to the hard-rod model, the inset shows that all curves collapse to a single line when $\phi$ and $r$ are rescaled by $\phi' = [\phi(r) - \phi(R)]/[\phi(0) - \phi(R)]$ and $r' = r/R$. (b) Probability density of the domain area, $P(A)$, for various values of the orientational stiffness $k_{F0}$. (c) The average domain area at a distance $r$ from the center of the colony. As in the hard-rod model, the typical domain area is uniform across the colony. (d) The average domain area for a colony scales linearly with the squared active length scale $\ell_a^2 = k_F/|\alpha|$. The inset shows that the radial distribution of domain areas can be rescaled by the squared active length scale to the same value. In presenting the results, we use $l = 1/\sqrt{\rho_c}$ as our units of length. We interpret the doubling time $t_g = \log(2)/k_g$ as the time per generation. The simulations were run on a $351 \times 351$ grid with the spacing set to 1. They start from a circle of bacteria with density $\rho_0 = 0.1$ and radius 6 grid points and grow to a given total mass, at which point the simulation ends. The (unscaled) parameters used were $\rho^* = 0.005$, $A_0 = 50$, $\rho_c = 0.1$, $\xi = 5$, $P_0 = 10$, $\lambda = 0.1$, and $\zeta = 10$. The two variable parameters are $\alpha_0 =$ (a) 0.225, (b) 0.45, (c) 0.225, and (d) $[0.225, 0.45]$, $k_{F0} =$ (a) 0.25, (b-c) $[0.15, 0.35]$, with $k_g = \alpha_0/25 - 0.0075$. Results presented are based on the average of 50 simulated colonies.

and $R \gg \sqrt{\mu/\kappa_g}$, which is the characteristic length scale associated with Eq. 3.12a. Thus, taking $\rho_c \to 0$ and $R \to \infty$, one can find an analytical solution of Eqs. 3.12 of the form

$$\rho(r,t) = \frac{M_0}{4\pi\mu t} \exp\left(k_g t - \frac{r^2}{4\mu t}\right) , \tag{3.13}$$

under the assumption that $\rho(\boldsymbol{r},0) = M_0\delta(\boldsymbol{r})$. Thus, in agreement with Eq. 3.2, we have

$$\frac{\rho(r,t)}{\rho(0,t)} \approx 1 - \left(\frac{r}{R}\right)^2 , \tag{3.14}$$

where, consistently with Eq. 3.12c, we have taken $R = 2\sqrt{\mu t}$. For generic $\rho_c$ and $R$ values, Eqs. 3.12 become analytically intractable; nonetheless, our numerical simulations (Fig. 3.9a) indicate that even the short time dynamics of the density $\rho$ is ultimately dominated by a similar competition between growth and drag.

The geometrical properties of the nematic microdomains are summarized in Figs. 3.9b–d. The area of the domains is exponentially distributed (Fig. 3.9b), and its average $\langle A \rangle_r$ is uniform across the colony (Fig. 3.9c) and proportional to the squared active length scale as demanded by Eq. 3.9 (Fig. 3.9d). The agreement between our discrete and continuous models not only validates our interpretation of the results presented in Secs. 3.1 and 3.2 but also demonstrates that the a growing bacterial colony can be described by the hydrodynamics theory of active nematics. On the one hand, this provides an efficient method to simulate growing bacterial colonies. Unlike discrete particle methods (including that used in section 3.1), our hydrodynamic approach does not suffer from the prohibitive slowdown caused by the exponential increase in the particle number, and it can be naturally generalized to other geometries and boundary conditions. On the other hand, this approach offers another prototype, i.e., growing bacterial colonies, for the experimental and theoretical study of active matter.

## 3.4 Experiment on *E. Coli* microcolony

To further test the significance of our results, we compare our theoretical predictions with experiments on a nonmotile strain of *E coli* NCM 3722 delta-motA. The cell-to-colony growth was observed on a 2-mm-thick layer of agarose gel uniformly mixed with LB, a nutritionally rich

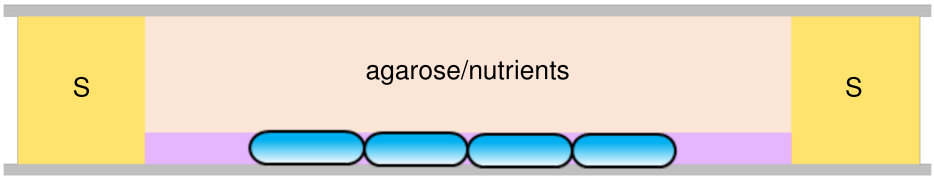


**Figure 3.10.** Lateral view of the micro-environment used in the bacterial growth experiments. *Escherichia coli* was grown on an agarose layer (pale pink) replete with Lysogeny broth (LB). The nutrient-rich agarose layer was sandwiched between two glass slides (grey hue) and enclosed with a 2-mm-thick neoprene spacer (marked as "S" in yellow). The cells (shown in blue) were imaged from below using time-lapse phase-contrast microscopy.

medium commonly used for growing bacteria (Fig. 3.10). The nutrient layer was sandwiched between two glass slides and enclosed within a 2-mm-thick neoprene spacer. The cells were imaged from below using time-lapse phase-contrast microscopy. For each experiment, we cultured the cells overnight in the LB medium. A dilute concentration of this culture was used to spot single bacterium on the agarose surface, which subsequently grew into colonies. For each experiment, *E. coli* was cultured overnight in the LB medium at 25 °C. A dilute concentration of this culture was then used to spot single bacterium on the agarose surface, which served as nucleating sites for subsequent colonies.

Under the given experimental conditions, the average doubling time of bacteria was $43.5 \pm 2.2$ minutes (doubling time for each replicate in minutes was 42.86, 45.89, 44.42, and 40.76). Cells in the colony were $0.9 \pm 0.1$ $\mu$m wide, while the average cell length varied among different colonies. The four replicates considered here were obtained under room-temperature conditions, which was stable at approximately 22° during the course of the measurements. The variability in the cell division lengths is frequently observed within colonies growing under similar conditions, potentially because of the inherent variability in the probability of growth itself (also known as phenotypic heterogeneity) [100]. Statistics were measured over four independent colonies. The nutrient-rich agarose layer was thus sufficiently thicker than the bacterial monolayer ($\simeq 1$ $\mu$m), which ensured constant availability of nutrients during the entire duration of the experiments.

We used time-lapse phase-contrast microscopy to visualize the growth of two-dimensional bacterial colonies (Fig. 3.1a–d). Images were acquired

using an Andor iXon Ultra 897 camera (8 $\mu$m/px) coupled to an inverted microscope (Nikon TE2000) with a 40$\times$ air objective (additional 1.5$\times$ magnification was used in some cases). This gave us a resolution of 0.2 $\mu$m (0.13 $\mu$m with additional 1.5$\times$ magnification). For a 4-$\mu$m-long cell, this resulted in a resolution of 20 pixels/cell. Using subpixel resolution (achieved by Gaussian interpolation), we could further improve this by a factor 2, which provided us with sufficient resolution to reliably detect and segment single cells. As checks, we analyzed the correct segmentation area over the entire segmented area (true positive rate) and, as a complementary parameter, looked at the false-positive rates. Prior to time-lapse image acquisition, we identified and recorded multiple spots on the agarose layer where single bacterium was present. The microscope was automated to scan these prerecorded coordinates and to acquire, every 3 minutes, the images of gradually growing bacterial colonies. By recording the phase-contrast images over hours, we acquired the necessary data for quantifying growing bacterial colonies. We analyzed the phase contrast images to extract the dimensions (length and width), position (centroid), and the orientation of each cell using intensity thresholding routines available through open source image analysis software ImageJ. Upon extraction of the cell dimensions, and the corresponding centroids and orientations, we generated orientation maps of the colony using MATLAB (MathWorks). All experiments were designed and conducted by Anupam Sengupta, while analyses of experimental data were done by Zhihong You.

Four independent colonies were cultured under the same experimental conditions as specified in the previous section. Despite their approximately similar doubling time, variance in their growth rates (rate of elongation) was quite significant, as was the variance in their division lengths. Figures 3.11a and 3.11b show two examples of proliferating colonies of cells, each with different division lengths and, hence, different cell aspect ratios. Like in the simulations, cells self-organize into nematic domains of different sizes and shapes, and the typical domain area increases with the cell aspect ratio. Along the colony boundary, the cells are preferentially oriented along the tangential direction, whereas in the bulk, the domains are isotropically oriented (insets in Fig. 3.11).

For the strain of bacteria we used, the division rate (or doubling time) is constant at a given temperature; hence, the growth rate (rate of elongation) is approximately proportional to the cell aspect ratio [55]. It is thus difficult to vary the growth rate and the cell aspect ratio independently

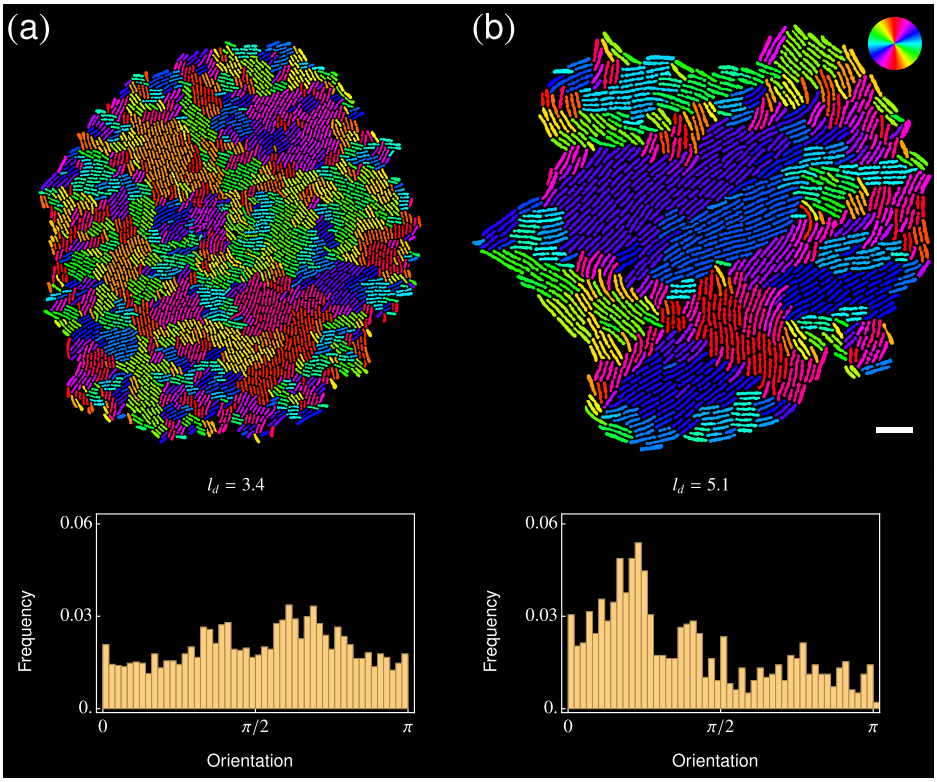


**Figure 3.11.** Snapshots of two-dimensional bacterial colonies with division lengths (a) $l_d = 3.4$ and (b) $l_d = 5.1$. Cells are color-coded with the same method as in Fig. 3.1, and the scale bar corresponds to 10 $\mu$m. The insets show the normalized frequencies of cell orientations of the corresponding colonies.

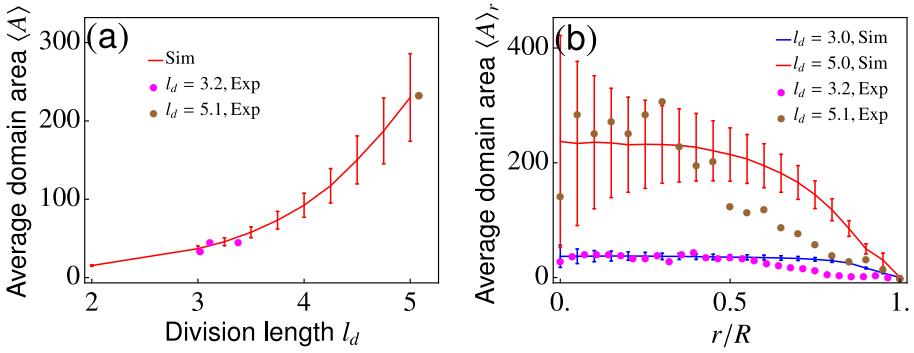


**Figure 3.12.** Comparisons between the experiments and the simulations in (a) average domain area $\langle A \rangle$ as a function of division length $l_d$, (b) spatial distribution of domain area $\langle A \rangle_r$. Data from four independent colonies in the experiment are analyzed, each corresponding to a dot in panel (a). Magenta dots represent results from three experimental colonies ($l_d = 3.4, 3.1, 3.0$ and $g = 3.1\mu$m/h, $2.9\mu$m/h, $2.8\mu$m/h in physical units) with an average division length $l_d = 3.2$, and the brown dots are from one experimental colony with division length $l_d = 5.1$ and growth rate $g = 4.2\mu$m/h in physical units. The simulation data, represented by solid lines, are the same as those shown in Figs. 3.3a–c, i.e., with a growth rate $g = 0.0002$ (or $4\mu$m/h in physical units).

in our experiment, as done in the simulations. However, as we can see from Figs. 3.3c and 3.3d, the variation of domain size is more sensitive to the division length $l_d$, if $l_d$ and $g$ are linearly related. For this reason, we compare the experimental results with those of a fixed growth rate from the MD simulations.

Figure 3.12a shows the average domain sizes of the four colonies (each represented by a dot) as a function of the division length $l_d$. We can see that the average domain sizes $\langle A \rangle$ in experiments fall well within the region predicted by our simulations. The spatial distribution of domain size, i.e., $\langle A \rangle_r$, is approximately constant for $l_d = 3.2$ (magenta dots in Fig. 3.12b), and overlaps well with that for $l_d = 3.0$ from the simulations. Here, $\langle A \rangle_r$ for $l_d = 5.1$ (brown dots in Fig. 3.12b) is also in the expected region. Note that $\langle A \rangle_r$ drops at a smaller $r/R$ in the experiments. This is because the colony radius $R$ is smaller in the experiment, and the relative thickness of the boundary layer, which contains smaller domains, is larger.

Because of the limited statistics, our experimental results do not allows us to formulate conclusive statements. However, the quantitative agree-

ment between the experiment and theory, is encouraging in suggesting that some of the geometrical and mechanical aspects of bacterial microcolonies can indeed be conceptualized in the framework of active liquid crystals.

## 3.5 Discussion and conclusion

Sessile bacteria communities have the extraordinary ability to colonize a variety of surfaces, even in the presence of nonoptimal environmental conditions. Such a process typically starts from a few or even a single cell that elongates and eventually divides at a constant rate, and this gives rise to highly complex two-dimensional and three-dimensional structures consisting of tightly packed and partially ordered cells. Colonies originating from a single bacterium initially develop in the form of a flat and circularly symmetric monolayer and, after reaching a critical population, invade the three-dimensional space forming stacks of concentric disk-shaped layers [61, 56]. While in the monolayer form, bacterial colonies exhibit prominent nematic order; however, this does not propagate across the colony, and it remains confined to a set of microscopic domains of coaligned cells. Using molecular dynamics simulations, continuous modeling and, to a limited extent, experiments on *E. coli* microcolonies, we have demonstrated that these domains originate from the interplay of two competing forces. On the one hand, the steric forces between neighboring cells favor alignment. On the other hand, the extensile active stresses due to growth tend to distort the system and disrupt the local orientational order. This results in an exponential distribution of the domain area, with a characteristic length scale $\ell_{\mathrm{a}} = \sqrt{k_F/|\alpha|}$, where $k_F$ is the orientational stiffness of the nematic domains and $\alpha$ the magnitude of the deviatoric active stress.

Previous studies have shown theoretically that random cell division in cellular monolayers can potentially induce an extensile active stress [63, 87]. By modeling the growing cellular monolayers as nematic liquid crystals, and coupling the nematic tensor $\boldsymbol{Q}$ with the local cell concentration $c$, they demonstrated that random cell division could locally increase the cell concentration and, through the $\boldsymbol{Q}$ coupling, drive a corresponding increase in the local nematic order. Changes in the local nematic order lead to the variations in the molecular field $\boldsymbol{H}$, and subsequently generate an extensile active stress of the form $\alpha\boldsymbol{Q}$. These results, though interesting, are grounded on the specifically designed yet unjustified coupling

between $\boldsymbol{Q}$ and the cell concentration $c$, as well as the fact that cell division has to be randomized in both space and time. In addition, works on sessile bacterial colony also revealed, in a qualitative picture, that cell growth could lead to an axial compression of cells, which could trigger a buckling instability of cell orientation, either in colonies confined in a straight channel [59], or at the interface between different species [53]. Here in this chapter, we systematically study the mechanical effects of cell growth in a freely expanding monolayer. With quantitative measurements and mathematical derivations, we demonstrate that cell growth can differentiate the normal components of the internal stress which, upon rearrangement, contains explicitly an extensile active stress $\alpha\boldsymbol{Q}$. The hydrodynamic theory introduced here, can then be used as a comprehensive framework to study the interplay among mechanical stresses, cell orientation, and the flow of cells, in growing bacterial colonies.

In addition, the present work allows an accurate description of the chaotic dynamics with a number of experimentally testable predictions, such as the exponential distribution of the domain area, summarized by Eq. 3.1, and the dependence of the average domain area on the cell aspect ratio and growth rate (Figs. 3.3c and 3.3d). The identification of the active length scale $\ell_{\mathrm{a}}$ offers a coherent interpretation of the collective behavior of the freely expanding monolayer. As active nematic liquid crystals, colonies of nonmotile duplicating bacteria are expected to be found in either an ordered or disordered state depending on the ratio between $\ell_{\mathrm{a}}$ and the colony size $R$. During the initial expansion ($R \ll \ell_{\mathrm{a}}$), the colony develops a highly aligned state, as the restoring forces arising in response to the elastic distortions outweigh the growth-induced active forces. Consequently, the collective growth of cells along the aligned direction results in an elongated shape of the colony (Figs. 3.1f and 3.1j). For a large colony ($R \gg \ell_{\mathrm{a}}$), on the other hand, the system is orientationally disordered and dynamically chaotic. The absence of preferred orientation renders the colony morphology isotropic (Figs. 3.1h and 3.1l).

Even though cell morphology is one of the most well-documented phenotypic traits of microorganisms, its role as a functional trait in microbial ecology and evolution has received little attention [101]. The spontaneous creation of microdomains during the initial stages of colony growth presents a remarkable setting, one in which *nonmotile* bacterial cells collectively lead to *emergent motility* within the colony, as visualized in the chaotic fracture and coarsening dynamics of the nematic domains. Con-

sequently, this interplay between growth-induced stresses and phenotypic stiffness of the participating cells introduces a novel angle to the transport and material attributes of such biologically active matter. Future studies on emergent motility within colonies of nonmotile cells, both in experiments and theory, are expected to contribute to a comprehensive biomechanical picture, highlighting the activity-driven cell-cell communications that precede biofilm formation. Finally, the results presented here are general and can be extended beyond bacterial communities, for instance, to study mammalian cells, many of which exist as nonmotile elongated phenotypes [102].